

# Regional Assessment of Cardiac Left Ventricular Myocardial Function via MRI Statistical Features

Mariam Afshin\*, Ismail Ben Ayed, Kumaradevan Punithakumar, Max Law, Ali Islam, Aashish Goela, Terry Peters, and Shuo Li

**Abstract**—Automating the detection and localization of segmental (regional) left ventricle (LV) abnormalities in magnetic resonance imaging (MRI) has recently sparked an impressive research effort, with promising performances and a breadth of techniques. However, despite such an effort, the problem is still acknowledged to be challenging, with much room for improvements in regard to accuracy. Furthermore, most of the existing techniques are labor intensive, requiring delineations of the endo- and/or epi-cardial boundaries in all frames of a cardiac sequence. The purpose of this study is to investigate a real-time machine-learning approach which uses some image features that can be easily computed, but that nevertheless correlate well with the segmental cardiac function. Starting from a minimum user input in only one frame in a subject dataset, we build for all the regional segments and all subsequent frames a set of statistical MRI features based on a measure of similarity between distributions. We demonstrate that, over a cardiac cycle, the statistical features are related to the proportion of blood within each segment. Therefore, they can characterize segmental contraction without the need for delineating the LV boundaries in all the frames. We first seek the optimal direction along which the proposed image features are most descriptive via a linear discriminant analysis. Then, using the results as inputs to a linear support vector machine classifier, we obtain an abnormality assessment of each of the standard cardiac segments in real-time. We report a comprehensive experimental evaluation of the proposed algorithm over 928 cardiac segments obtained from 58 subjects. Compared against ground-truth evaluations by experienced radiologists, the proposed algorithm performed competitively, with an overall classification accuracy of 86.09% and a kappa measure of 0.73.

Manuscript received July 25, 2013; accepted August 19, 2013. Date of publication October 30, 2013; date of current version nulldate. *Asterisk indicates corresponding author.*

\*M. Afshin is with the Robarts Research Institute, London, ON, N6A 5K8 Canada, and also with the Department of Biomedical Engineering, University of Western Ontario, London, ON, N6A 5B9 Canada (e-mail: mafshin@robarts.ca).

I. B. Ayed is with GE Healthcare, London, ON, N6A 4V2 Canada, and also with the Department of Medical Biophysics, The University of Western Ontario, London, N6A 5C1 Canada.

K. Punithakumar is with the Servier Virtual Cardiac Centre, Mazankowski Alberta Heart Institute, Edmonton, AB, T6G 2P4 Canada, and also with the Department of Radiology and Diagnostic Imaging, The University of Alberta, Edmonton, AB, T4V 2R3 Canada.

M. Law is with the Department of Medical Biophysics, University of Western, London, ON, N6A 5C1 Canada.

A. Islam is with the Department of Radiology and Diagnostic Imaging, St. Joseph's Health Care, London, ON, M6R 1B5 Canada.

A. Goela is with the Department of Radiology and Diagnostic Imaging, London Health Science Center, London, ON, M6R 1B5 Canada.

T. Peters is with the Robarts Research Institute, London, ON, N6A 5K8 Canada, and also with the Department of Biomedical Engineering, The University of Western Ontario, London, ON, N6A 5B9 Canada.

S. Li is with GE Healthcare, London, ON, N6A 4V2 Canada and also with the Department of Medical Biophysics, The University of Western Ontario, London, ON, N6A 5C1 Canada.

Color versions of one or more of the figures in this paper are available online at <http://ieeexplore.ieee.org>.

Digital Object Identifier 10.1109/TMI.2013.2287793

**Index Terms**—Bhattacharyya coefficient, image statistics, linear discriminant analysis (LDA), linear support vector machine (LSVM), magnetic resonance imaging (MRI), regional wall motion abnormality detection.

## I. INTRODUCTION

EARLY and accurate detection of segmental (regional) left ventricle (LV) abnormalities in magnetic resonance imaging (MRI) is widely accepted as a predictor of cardiac diseases, the leading cause of death worldwide [1]. In routine clinical procedures, segmental cardiac function is considered an essential diagnosis and follow-up component [2]. It is often assessed *visually* following the American Heart Association (AHA) [3] standard, which prescribes selecting representative 2-D cardiac slices so as to generate 17 standardized LV segments. Based mainly on visual assessments, current radiologic practices are subject to high inter-observer variability [4], [5], and are subjective and nonreproducible. For instance, the clinical study in [4] showed that the mean kappa measure of detecting regional wall motion abnormalities by three different radiologists could be as low as 0.43. The difficulties come from the subtle visual differences between normal- and abnormal-segment motions. Alternatively, automating the detection and localization of regional abnormalities has recently sparked an impressive research effort [6]–[11], with promising performances and a breadth of techniques. However, despite such efforts, the problem is still acknowledged challenging, with the need for significant improvements in accuracy. For instance, the recent publication in [8] reports an accuracy of 63.70% (base), 67.41% (middle), and 66.67% (apex) when visual wall motion scoring is used as reference.

### A. Prior Art

Most of the pioneering studies of wall motion abnormality detection targeted echocardiography [12]–[14], using concepts from shape statistics [12], [13] and hidden Markov models [14], among others. More recently, MRI-based wall motion abnormality detection has attracted significant research attention [6]–[11]. In [10], Punithakumar *et al.* characterized myocardial-segment motions via a nonlinear dynamic model, and used the Shannon's differential entropies of various segment features (e.g., areas and radial distances) as inputs of a naive Bayes classifier. In [13], Leung and Bosch built sparse shape models with localized variations from four- and two-chamber echocardiographic sequences using principal component analysis and orthomax rotations. The ensuing shape parameters were then

used to assess local wall motion. In [8] and [15], Suinesiaputra *et al.* built normokinetic myocardial shape models using short-axis MR images acquired from healthy volunteers. Then, they proposed to use an independent component analysis (ICA) classifier that detects and localizes abnormally contracting segments, via a characterization of local shape variations. Lekadir *et al.* [11] focused on statistical modeling based on spatio-temporal inter-landmark relationships. In [7], Lu *et al.* proposed a pattern recognition technique built upon intra-segment correlation, using a normalization scheme that maps each LV slice to polar coordinates with fixed size, intensity level, and position. The study in [9] proposed a differentiable-manifold analysis, following differential geometry concepts to define a parameterization of the LV domain which is considered as a deforming manifold. The authors of [6] investigated a tensor-based linear discriminant analysis (LDA) classification that conserves the spatio-temporal structure of the myocardial function. Radial and circumferential strain as well as tissue-rotation angle were used as features to train and test a classifier via manual segmentations of the myocardium.

Most of the existing methods require delineations of the endo- and/or epi-cardial boundaries in all frames of a cardiac sequence, using either a manual time-consuming process [6]–[9] or an automatic/semi-automatic segmentation (delineation) algorithm [16], which is itself a challenging and computationally expensive task that may result in high estimation errors [16]. In general, segmentation algorithms require either careful user interventions and/or intensive manual training, along with a heavy computational load. Furthermore, the ensuing segmentation results often hinge on the choice of a large set of *ad hoc* parameters and training data, which may yield high errors. These difficulties inherent to segmentation algorithms might impede significantly segmental motion abnormality detection. Moreover, some of the existing algorithms, e.g., those based on shape analysis techniques [8], require such delineations in the training phase, which increases significantly the amount of manual inputs and training complexity.

### B. Contributions of This Paper

While existing techniques are labor intensive, we believe that there are other characteristics of the images that can be computed with less effort, but that nevertheless correlate with the segmental cardiac function. One such technique that we describe below is based on image features and machine learning.

The main contribution of this work is in building statistical image features that do not require segmentations and can be easily computed, but that can characterize well segmental cardiac function. The new features remove the need for delineating the endo- and epi-cardial boundaries in all the images of a cardiac sequence. Starting from a minimum user input in a single frame of subject data, we build for all the regional segments and all subsequent frames a set of statistical MRI features based on a measure of similarity between distributions. We demonstrate that, over a cardiac cycle, the statistical features are related to the proportion of blood within each segment. These features can therefore characterize segmental contraction without the need

for delineating the LV boundaries in all the frames. We first seek the optimal direction along which the proposed image features are most descriptive via a LDA. Then, using these results as inputs to a linear support vector machine (LSVM) classifier, we obtain an abnormality assessment of each of the standard cardiac segments in real-time. We report a comprehensive experimental evaluation of the proposed algorithm over 928 cardiac segments obtained from 58 subjects. Using evaluations by experienced radiologists as ground-truth, the proposed algorithm yielded a competitive performance, with an overall classification accuracy of 86.09% and a kappa measure of 0.73.

A preliminary conference version of this work appeared in MICCAI 2011 [17]. This journal version expands on [17] with 1) a wider experimental investigation that includes more patient data, radiologist assessments, and statistical validations; and 2) a much broader, more informative/rigorous discussion of the subject.

## II. IDENTIFYING 16 SEGMENTS IN ONLY ONE FRAME

This step requires a user-provided delineation of the endo- and epicardium boundaries in only one single frame, which we refer to as the *reference* frame. Following the AHA standard [3], we use such a simple user input to divide the heart into 16 standard segments. Then, we superimpose the obtained segments systematically (without additional user effort) to all the other frames.

Constructing the 16 segments follows standard AHA prescriptions [3], and is based on the following steps.

- Dividing the LV into equal thirds perpendicular to the long axis of the heart, thereby generating three circular LV sections: apical [Fig. 1(a)], mid-cavity [Fig. 1(b)], and basal [Fig. 1(c)]. As prescribed in [3], we use only three representative slices containing the myocardium in all  $360^\circ$ .
- Dividing the basal part into six segments of  $60^\circ$  each, as shown in Fig. 2(c). We used the attachment of the right ventricular wall to the LV (septal wall) as anatomical landmark to identify the septum.
- Dividing the apical part into four segments of  $90^\circ$  each, as shown in Fig. 2(a).
- Dividing the mid-cavity part is into six segments of  $60^\circ$  each, as shown in Fig. 2(b).

## III. CONSTRUCTING STATISTICAL FEATURES FROM MRI IMAGES

We propose to use image statistics as input features to classify regional myocardial segments into normal and abnormal.

### A. A Synthetic Example

Let us first describe the concept for the simple synthetic-motion example in Fig. 3. The example depicts several frames, each containing two regions, a white disc (which we denote region  $x_j$ ) and a black ring enclosing  $x_j$  (which we denote region  $y_j$ );  $j$  is an integer denoting the frame number ( $j \geq 1$ ).

During a simulated cardiac cycle, region  $x_j$  is shrinking and expanding, mimicking the LV blood cavity during a cardiac

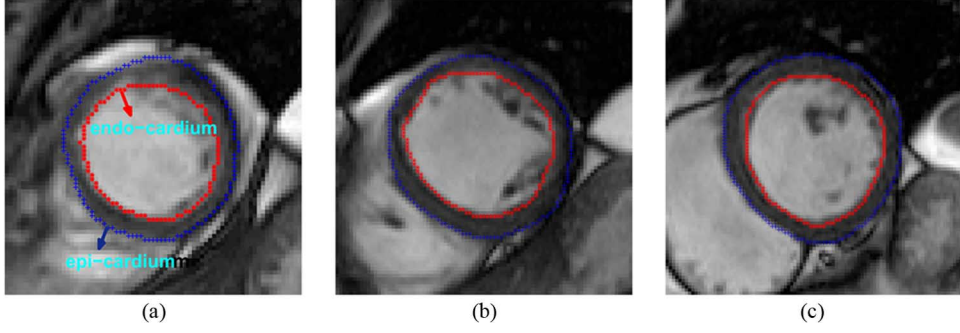


Fig. 1. User-provided delineation in one single frame (reference image  $I_s$ ) for three representative slices: (a) apical, (b) mid-cavity, and (c) basal.

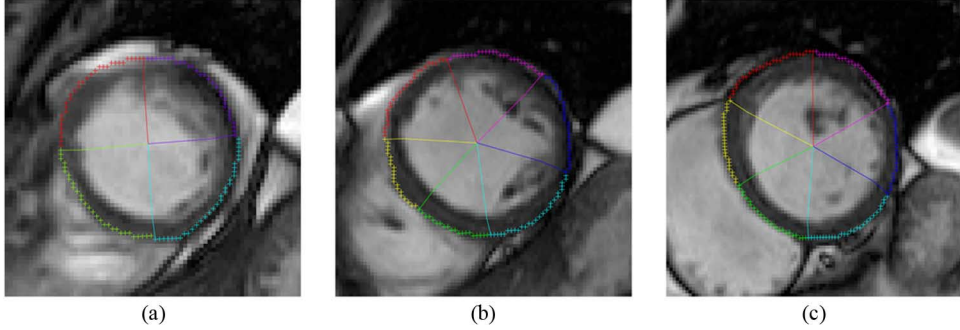


Fig. 2. Regional segments superimposed on reference image  $I_s$ . (a) Apical. (b) Mid-cavity. (c) Basal.



Fig. 3. Simple synthetic example which demonstrates how some segmentation-free image statistics correlate with the dynamics of a moving region.

cycle, whereas region  $x_j \cup y_j$  remains constant ( $x_j \cup y_j$  corresponds to the whole image domain  $\forall j$ ). Let  $Q_j$  denotes the intensity within frame  $j$

$$\begin{aligned} Q_j(p) &= 1 \quad \forall p \in x_j \\ Q_j(p) &= 0 \quad \forall p \in y_j. \end{aligned} \quad (1)$$

Let  $P(\cdot/x_j)$  and  $P(\cdot/x_j \cup y_j)$  denote the probability distributions of intensity within regions  $x_j$  and  $x_j \cup y_j$  respectively

$$\begin{aligned} P\left(Q_j = \frac{1}{x_j}\right) &= P\left(Q_1 = \frac{1}{x_1}\right) = 1 \quad \forall j \\ P\left(Q_j = \frac{0}{x_j}\right) &= P\left(Q_1 = \frac{1}{x_1}\right) = 0 \quad \forall j \\ P(Q_j = 1/x_j \cup y_j) &= \frac{a_j}{A} \quad \forall j \\ P(Q_j = 0/x_j \cup y_j) &= \frac{A - a_j}{A} \quad \forall j \end{aligned} \quad (2)$$

where  $a_j$  denote the area of region  $x_j$  within time frame  $j$ , and  $A$  the area of the image domain.

Now let us consider the Bhattacharyya coefficient [18] that measures the amount of overlap (similarity) between two distributions  $f$  and  $g$

$$\mathbf{B}_{\mathbf{Z}}(f, g) = \sum_{z \in \mathbf{Z}} \sqrt{f(z)g(z)} \quad (3)$$

where  $\mathbf{Z}$  is the set of values over which the distributions are defined. For this synthetic example,  $\mathbf{Z} = \{0, 1\}$ . Note that the range of the Bhattacharyya coefficient is  $[0, 1]$ , with 0 indicating no overlap between the distributions and 1 indicating a perfect match.

Let us assume that we have a segmentation (delineation) of region  $x$  in only one frame (the first frame), i.e., only  $x_1$  is known (for  $j \geq 2$ ,  $x_j$  is not segmented). For each  $j \geq 2$ , we can show that the following image statistic is directly related to the area of region  $x_j$ :

$$\begin{aligned} \mathbf{B}_{\{0,1\}}(P(\cdot/x_1), P(\cdot/x_j \cup y_j)) \\ = \sqrt{0 \times P(0/x_j \cup y_j) + 1 \times P(1/x_j \cup y_j)} = \sqrt{\frac{a_j}{A}}. \end{aligned} \quad (4)$$

Notice that the computation of the image statistic in the left-hand side of (4) does not need a segmentation of  $x_j$  for  $j \geq 2$ . This image statistic depends only on  $x_1$  and the entire image  $x_j \cup y_j$ . Recall that region  $x_j \cup y_j$  remains constant for all frames ( $x_j \cup y_j$  corresponds to the whole image domain  $\forall j$ ) and only region  $x_j$  is shrinking and expanding. Nonetheless, the expression in the right-hand side is related to the areas of regions  $x_j$  and, therefore, contains information about the dynamics of these regions. This makes sense because the more overlap between the distribution of region  $x_j$  and the whole image, the larger the proportion of pixels within region  $x_j$ .

We will use this concept to build cardiac-segment statistics that correlate well with regional LV function, while removing the need for comprehensive segmentations of all the images in a cardiac sequence.

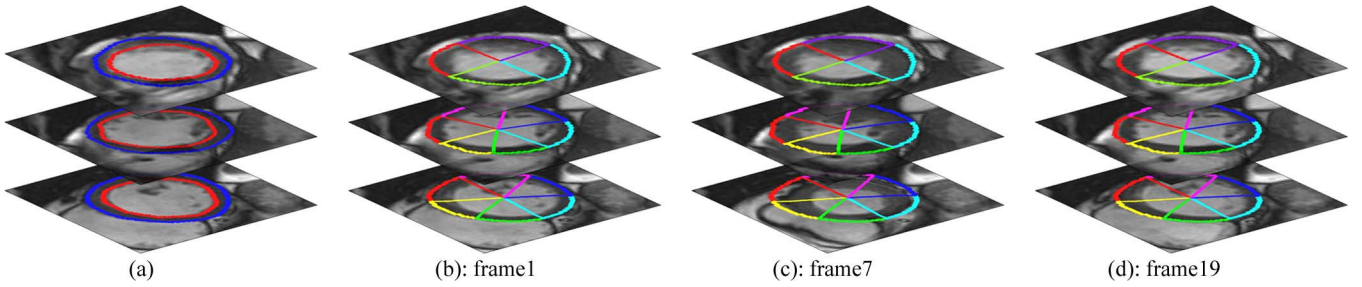


Fig. 4. (a) Manual segmentation of the reference (end-diastolic) frame. (b) Regional segments of the reference frame. (c), (d) Regional segments of the reference frame superimposed systematically (without additional user effort) onto the rest of the frames.

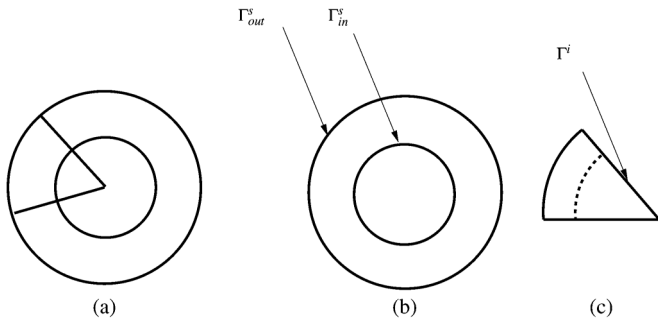


Fig. 5. (a) Reference image  $\mathbf{I}_s$ . (b) Endo- and epi-cardial boundaries in  $\mathbf{I}_s$ . (c) Boundary of regional segment  $i$  in the reference frame.

### B. Building Segmental Image Statistics for Cardiac MRI Images

Let  $\mathcal{I}$  be a cardiac MRI sequence containing  $J$  frames,<sup>1</sup> each comprising  $S$  slices<sup>2</sup>  $\mathcal{I}_{s,j}: \Omega \subset \mathbb{R}^2 \rightarrow \mathbb{R}^+$  with  $(s, j) \in [1 \dots S] \times [1 \dots J]$ . For each frame, we have  $I$  regional segments<sup>3</sup>  $\mathcal{K}_{i,j}$ , with  $(i, j) \in [1 \dots I] \times [1 \dots J]$ .

Let us first consider the following basic definitions and notations.

- $\mathbf{I}$  is the reference frame, which consists of three 2-D images,  $\mathbf{I}_s$ ,  $s = 1, \dots, 3$ , each associated with a different slice level (apical, basal, and mid-cavity). The reference frame corresponds to the end-diastolic phase.
- Let  $\Gamma_{\text{in}}^s, \Gamma_{\text{out}}^s: [0, 1] \rightarrow \Omega$  denote the endo- and epi-cardial boundaries in  $\mathbf{I}_s$ , respectively [refer to Fig. 4(a)].
- Let  $\Gamma^i: [0, 1] \rightarrow \Omega$  denotes the boundary of regional segment  $i$  in the reference frame (refer to Fig. 5 for an illustration).

Now, for each  $i$ , let us superimpose systematically (i.e., without additional user effort) segment boundary  $\Gamma^i: [0, 1] \rightarrow \Omega$  onto the remaining frames as shown in Fig. 4, and compute the corresponding image statistics (Figs. 6–8).

To formally introduce the expression of the image statistic for each regional segment at each time step, let us consider the following general definitions.

- Let  $\mathbf{R}_\Gamma \subset \Omega$  denote the region enclosed within curve  $\Gamma$ ,  $\Gamma \in \{\Gamma_{\text{in}}^s, \Gamma_{\text{out}}^s, \Gamma^i\}$ .

<sup>1</sup> $J$  is typically equal to 20 or 25.

<sup>2</sup> $S$  is equal to 3; we used three representative slices following the AHA standard [3].

<sup>3</sup>The number of regional segments ( $I$ ) per subject is equal to 16.

- Let  $P_{\mathbf{R},A}$  denote the kernel density estimate of the distribution of an image  $A$  within region  $\mathbf{R}$

$$P_{\mathbf{R},A}(z) = \frac{\int_{\mathbf{R}} K(z - A(x)) dx}{a_{\mathbf{R}}} \quad \forall A \in \{\mathcal{I}_{s,j}\},$$

$$(s, j) \in [1 \dots S] \times [1 \dots J] \quad (5)$$

where  $a_{\mathbf{R}}$  is the area of region  $\mathbf{R}$

$$a_{\mathbf{R}} = \int_{\mathbb{R}^+} dx \quad (6)$$

and  $K$  is the Gaussian kernel [19]

$$K(y) = \frac{1}{\sqrt{2\pi\sigma^2}} \exp^{-\frac{y^2}{2\sigma^2}}. \quad (7)$$

We assume the following.

- The reference-image distribution within the region inside  $\Gamma_{\text{in}}$  ( $P_{\mathbf{R}_{\Gamma_{\text{in}}}, \mathbf{I}_s}$ ) approximates the cavity distribution.
- The distribution of each image  $\mathcal{I}_{s,j}$  within  $\Gamma^i$  approximates the image distribution within regional segment  $\mathcal{K}_{i,j}$ , i.e.,

$$P_{\mathbf{R}_{\Gamma^i}, \mathcal{I}_{s,j}} \approx P_{\mathcal{K}_{i,j}, \mathcal{I}_{s,j}}. \quad (8)$$

As we shall see shortly, this approximation can be effectively used to compute, without the need for segmentation, an image statistic that correlates well with the amount of blood within segment  $\mathcal{K}_{i,j}$ .

Now, as a statistical feature for each regional segment  $\mathcal{K}_{i,j}$ , we consider the following Bhattacharyya similarity measure between distributions

$$\beta^{i,j} = \mathbf{B}_{\mathbb{R}^+} \left( P_{\mathbf{R}_{\Gamma_{\text{in}}}, \mathbf{I}_s}, P_{\mathbf{R}_{\Gamma^i}, \mathcal{I}_{s,j}} \right). \quad (9)$$

In a way conceptually similar to the synthetic example we discussed earlier, we expect that feature  $\beta^{i,j}$  is related to the proportion of blood within regional segment  $\mathcal{K}_{i,j}$ . We further demonstrate experimentally such a relationship by the typical examples in Figs. 6–8, which show that the more overlap (similarity) between the distributions of the cavity and regional segment  $\mathcal{K}_{i,j}$ , the larger the proportion of blood within the segment. Therefore, we anticipate that over a cardiac cycle, the set of features  $\beta^{i,j}$ ,  $j \in [1 \dots J]$ , can characterize segmental cavity contraction. Another way to see how features  $\beta^{i,j}$  can describe segmental function is to consider the extreme case where the regional segment does not move. In such case, the

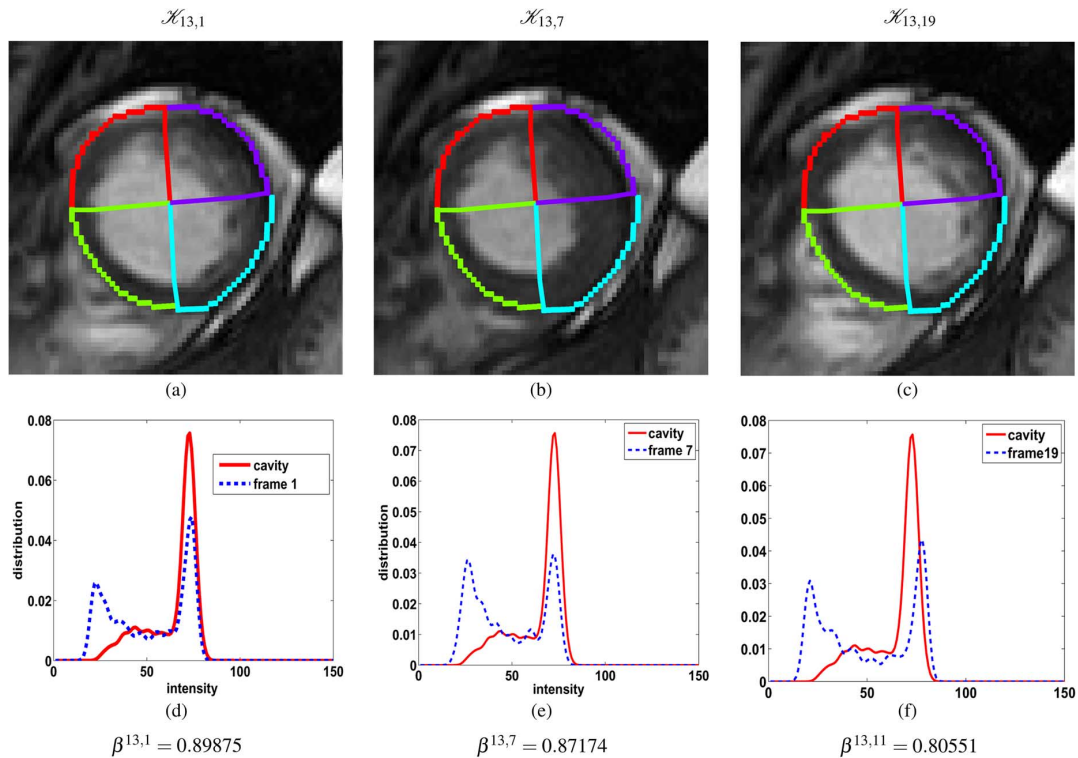


Fig. 6. (a)–(c) Regional myocardial segments of an apical slice superimposed on subsequent frames. (d)–(f) Image statistics corresponding to regional segment 13.

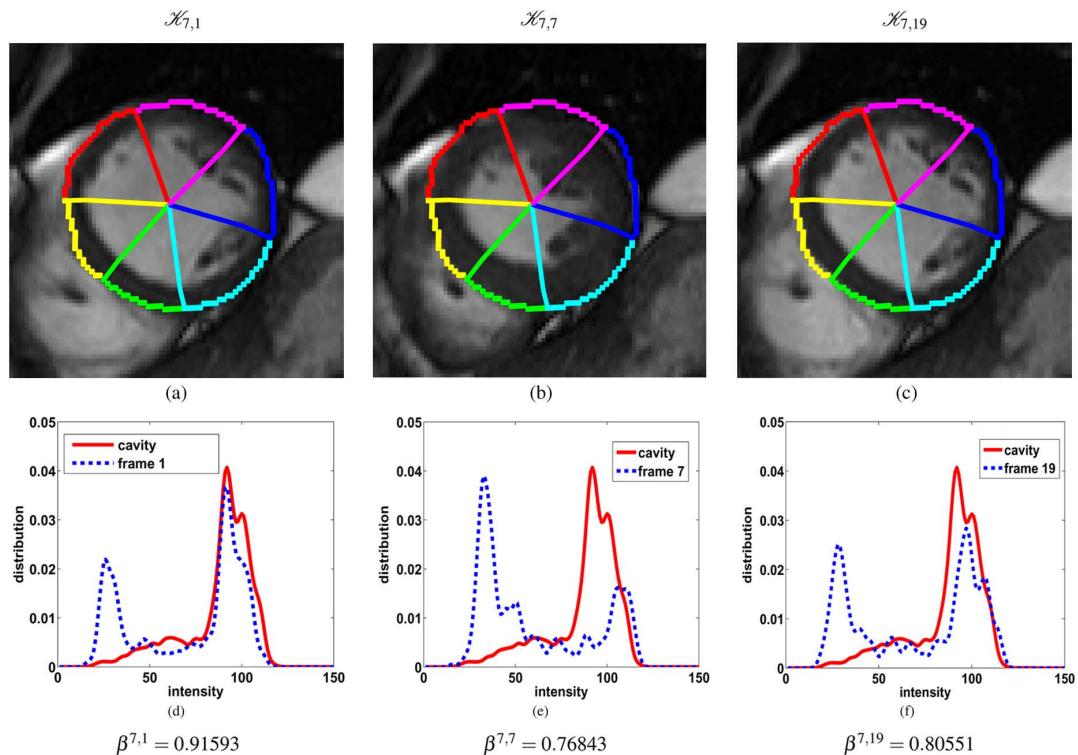


Fig. 7. (a)–(c) Regional myocardial segments of a mid-cavity slice superimposed on subsequent frames. (d)–(f) Image statistics corresponding to regional segment 7.

proportions of blood is constant over a cardiac cycle, and so are the features.

Fig. 9 summarizes the procedure for estimating the statistical image-based features.

#### IV. DIMENSIONALITY REDUCTION VIA LINEAR DISCRIMINANT ANALYSIS

The Bhattacharyya statistics from  $M$  training subjects can be viewed as a cloud of  $M$  points in the  $J$ -dimensional Euclidean

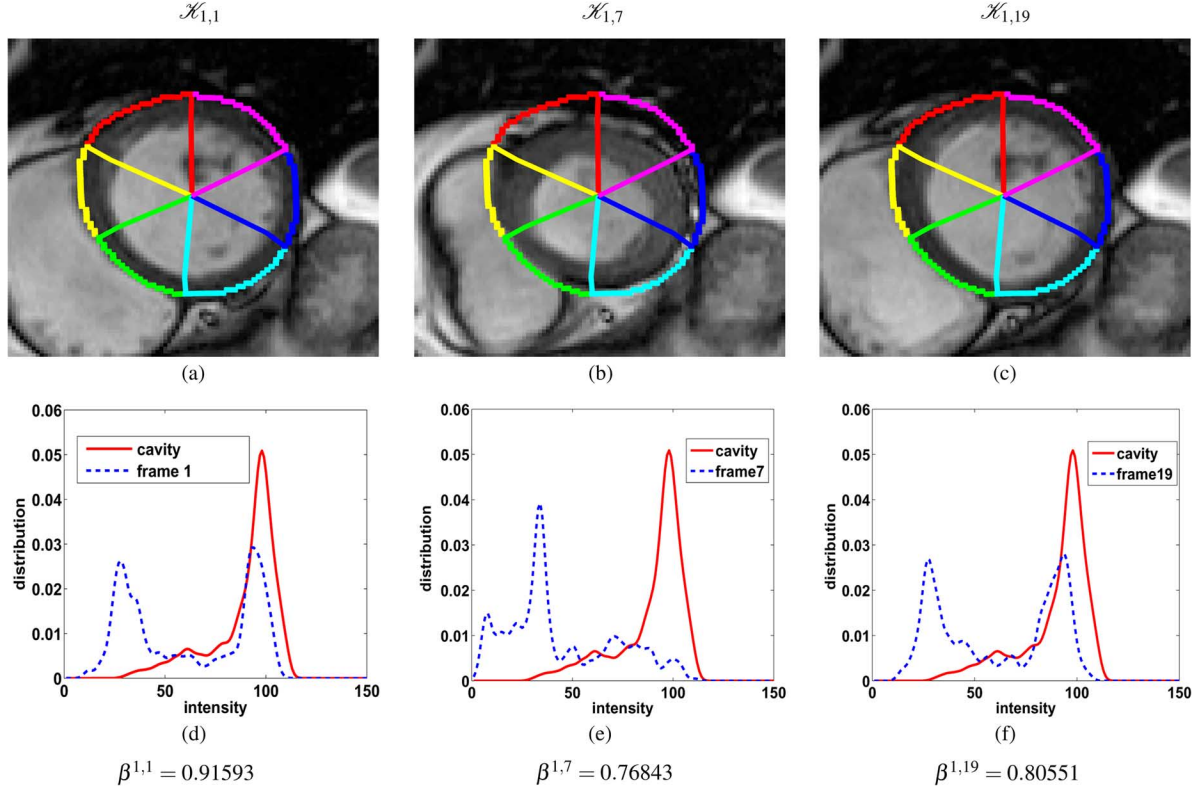


Fig. 8. (a)–(c) Regional myocardial segments of a basal slice superimposed on subsequent frames. (d)–(f) Image statistics corresponding to regional segment 1.

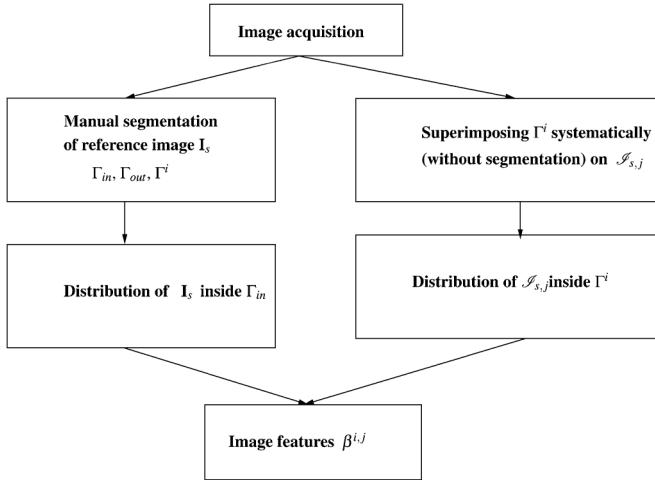


Fig. 9. Procedure of estimating the statistical image-based features.

space. We proceeded to a LDA [20]–[23] to reduce the dimensionality of the image features. Following LDA [20], one can assume that these points lie within a lower-dimensional space. Consider the following definitions and notations.

- Let feature vector  $\vec{\beta}_m^i = [\beta^{i,1}, \dots, \beta^{i,j}, \dots, \beta^{i,J}]$  be a  $J$ -dimensional row matrix containing the Bhattacharyya statistics for a given training subject  $m$ ,  $m \in \{1, \dots, M\}$ .
- Assume that each feature vector ( $\vec{\beta}_m^i$ ) belongs to one of two classes  $C_1$  and  $C_2$ , where  $C_1$  and  $C_2$  represent respectively normality and abnormality condition of the corresponding regional segment.

- Let  $\mu_e$  be the mean of feature vectors in class  $C_e$ ,  $e \in \{1, 2\}$

$$\mu_e = \frac{1}{N_e} \sum_{\vec{\beta}_m^i \in C_e} \vec{\beta}_m^i \quad (10)$$

where  $N_e$  is the number of the feature vectors in class  $C_e$ .

- Let  $\mu$  be the mean of all feature vectors

$$\mu = \frac{1}{M} \sum_{m=1}^M \vec{\beta}_m^i. \quad (11)$$

The between-class scatter matrix  $S_b$  [24] is defined as

$$S_b = \frac{1}{N} \sum_{e=1}^2 N_e (\mu_e - \mu) (\mu_e - \mu)^T \quad (12)$$

and the within-class scatter matrix [24]  $S_w$  is defined as

$$S_w = \frac{1}{N} \sum_{e=1}^2 \sum_{\vec{\beta}_m^i \in C_e} (\vec{\beta}_m^i - \mu_e) (\vec{\beta}_m^i - \mu_e)^T \quad (13)$$

where  $N$  is the number of the feature vectors in both classes.

In LDA [24], a projection vector  $G$  is chosen so as to maximize the following ratio:

$$G_{\text{opt}} = \operatorname{argmax}_G \frac{G^T S_b G}{G^T S_w G}. \quad (14)$$

Maximizing such a ratio seeks to reduce dimensionality while preserving as much of the class discriminatory information as possible. In the two-class case, LDA can only produce a scalar.

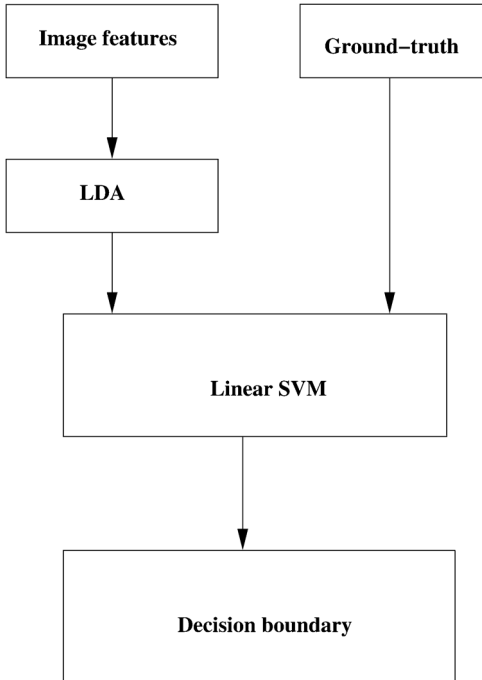


Fig. 10. Overview of the training phase.

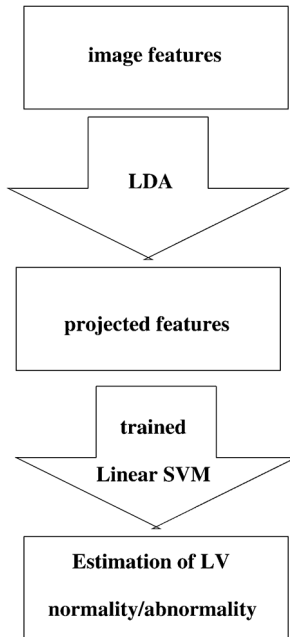


Fig. 11. Overview of the testing phase.

It finds a vector  $G_{\text{opt}} \in \mathbb{R}^{J \times 1}$  ( $1 \leq J$ ) that maps original data  $\vec{\beta}_m^i$  to a scalar  $\beta_{mp}^i$

$$G_{\text{opt}} : \vec{\beta}_m^i \in \mathbb{R}^J \rightarrow \beta_{mp}^i \in \mathbb{R}^1$$

$$\beta_{mp}^i = G_{\text{opt}}^T \vec{\beta}_m^i. \quad (15)$$

This amounts to projecting the data onto a line that maximizes the class separability of the scalars.

In the next step, we use a LSVM classifier to classify the projected features ensuing from a given testing subject into normal or abnormal. Fig. 10 summarizes the overall classification procedure.

## V. LINEAR SUPPORT VECTOR MACHINE CLASSIFICATION OF REGIONAL SEGMENTS

This step consists of classifying regional myocardial segments with a LSVM, given projected features  $\vec{\beta}_{mp}^i$  (refer to Fig. 11). Let  $(\vec{\beta}_{mp}^i, t_m)$ ,  $m = 1, \dots, M$ , be an annotated training set, with  $t_m$  denoting the labels associated with  $\vec{\beta}_{mp}^i$ . Variable  $t_m$  has two possible values ( $t_m \in \{-1, 1\}$ ), 1 corresponding to the abnormal-segment class and  $-1$  to the normal-segment class. The two-class LSVM classifier evaluates the sign of a linear function the form [25]–[29]

$$y(\mathbf{x}) = \mathbf{w}^T \phi(\mathbf{x}) + b \quad (16)$$

where  $\phi(\mathbf{x})$  denotes a fixed feature space, and  $b$  indicates a bias parameter. The sign of  $y(\mathbf{x})$  indicates the class of input  $\mathbf{x}$ . We assume that the training features are linearly separable, i.e., there exists at least one choice of  $b$  that satisfies  $y(\vec{\beta}_{mp}^i) \geq 0$  for features having  $t_m = +1$  and  $y(\vec{\beta}_{mp}^i) \leq 0$  for features having  $t_m = -1$ . SVM approaches this problem through the concept of the margin, which is defined to be the smallest distance between the decision boundary and any of the features (for an illustration, refer to [29, Fig. 7.1]). To find the decision boundary, we need to maximize the margin, i.e., the perpendicular distance characterizing the feature-point that is closest to the decision boundary [29]. Thus, the maximum-margin solution is sought by solving (17) (for further details, refer to [29, p. 327])

$$\text{argmax}_{\mathbf{w}, b} \left\{ \frac{1}{\|\mathbf{w}\|} \min_m [t_m (\mathbf{w}^T \phi(\vec{\beta}_{mp}^i) + b)] \right\}. \quad (17)$$

The direct solution to this optimization problem is quite challenging. However, one can resort to some assumptions and modifications so as to convert (17) into minimizing a quadratic function subject to a set of linear inequality constraints, which can be solved via a standard Lagrangian-multiplier method. Further details can be found in [29, Ch. 7].

We trained the LSVM classifier by providing the training-set features  $(\vec{\beta}_{mp}^i)$  and the corresponding ground-truth annotations  $t_m$  (Fig. 10 depicts an illustration). Then, the optimal hyperplane is computed by solving (17), and is used as a decision boundary to classify new (testing-subject) features into normal or abnormal segments.

## VI. EXPERIMENTS

### A. Data Acquisition

The data contain  $58 \times 3$  short-axis image datasets (i.e., apical, mid-cavity, and basal), each consisting of 20 functional 2-D images acquired from 21 normal and 37 abnormal hearts, using 1.5T MRI scanners with fast imaging employing a steady state

TABLE I  
DETAILS OF THE DATASETS USED IN THE EVALUATION  
OF THE PROPOSED METHOD

Description	Value
Number of subjects	58
Scanner protocol	FIESTA
Patient ages	16 – 79 years
Short-axis image resolution	(256 × 256) or (512 × 512) pixels
Number of frames (K)	20
Temporal resolution ( $\Delta T$ )	29 – 76 ms
Pixel spacing	(0.7 × 0.7 × 10.0) – (1.7 × 1.7 × 12.0) mm

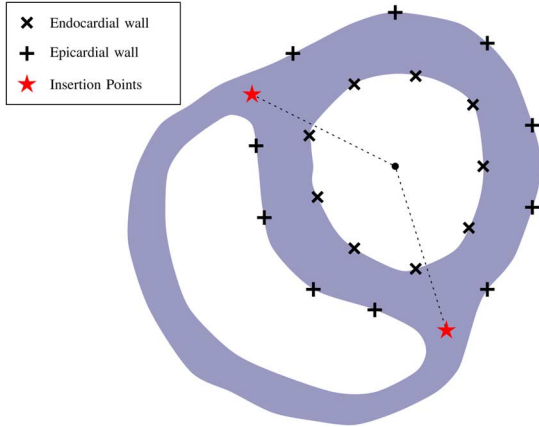


Fig. 12. User input to specify initial segmentation and anatomical landmarks on the first frame.

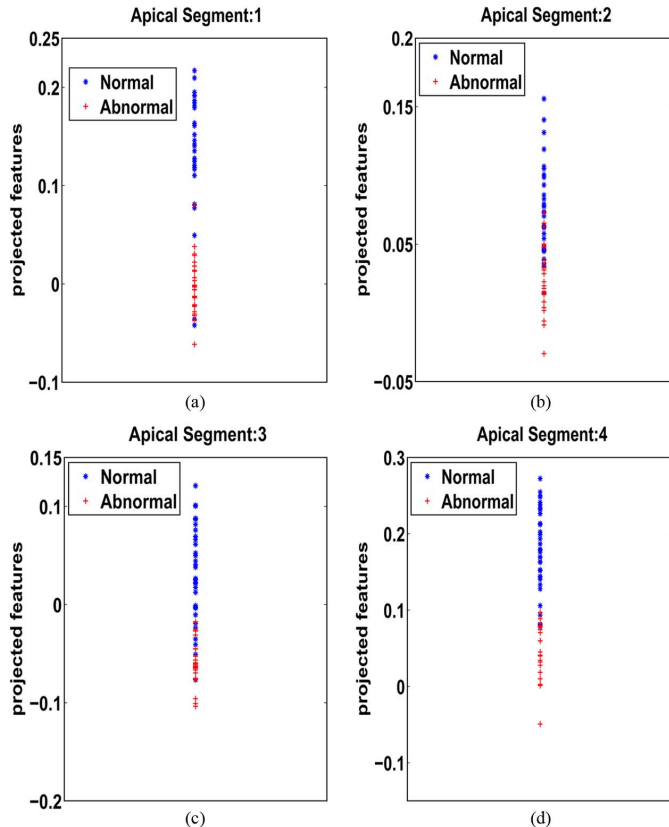


Fig. 13. Projected apical features ( $\beta_{mp}^i$ ) obtained following the LDA transformation.

acquisition (FIESTA) mode. The details of the datasets are presented in Table. I. The data consist of images from 41 male and 17 female subjects, and an average age of  $52.3 \pm 15.0$  years. The temporal resolution ( $\Delta T$ ) is  $45.1 \pm 8.8$  ms.

For each subject, slices were chosen from apical, mid-cavity and basal frames, and *anatomical landmarks* were identified manually on the first frame<sup>4</sup> (see Fig. 12 for an illustration). A cubic spline interpolation was used to sample  $N$  points along each endo- and epi-cardial boundary. The higher  $N$ , the better the estimation accuracy. However, the computational complexity of the algorithm increases with the values of  $N$ . The apical, mid-cavity and basal slices were automatically partitioned into 4, 6, and 6 segments, respectively, following the standard procedure outlined in [3], which results in 16 segments per subject. The 17th segment, apex, was not analyzed.

The results of 928 myocardial segments (58 subjects × 16 segments) were compared to a single ground truth classification.<sup>5</sup> We classify a segment as abnormal if that segment is hypokinetic, akinetic, or disketic. Among the 37 abnormal subjects, 12 were diagnosed with infarction, 10 with dilated cardiomyopathy, and 15 with various heart diseases including resuscitated cardiac arrest, coronary artery occlusion, cardioembolic cerebrovascular accident, and pseudo-aneurysm.

### B. Linear Discriminant Analysis

Figs. 13–15 show the projected features  $\beta_{mp}^i$  obtained following the LDA transformation for apical, mid-cavity, and basal segments. Fig. 13 demonstrates that the apical-segment transformation is more discriminative than those obtained for basal and mid-cavity segments. This can be explained by the fact that the image-distribution estimation within apical segments is not affected by the occurrences of papillary muscles in the blood pool.

### C. Linear SVM Classifier

We used 16 LSVM classifiers, each assessing one of the 16 standard segments (normal/abnormal). Figs. 16–18 show the decision boundaries that separate normal and abnormal classes. Fig. 16 depicts the projected features of four apical segments for each of the 58 subjects; the total number of apical segments is 232 (129 normal and 103 abnormal). Fig. 17 shows the projected features of a total of 348 mid-cavity segments (209 normal and 139 abnormal), where each of the 58 subjects has six mid-cavity segments. Fig. 18 depicts the projected features of 348 basal segments (221 normal and 127 abnormal). The larger the distance between the support vectors of normal and abnormal classes, the more reliable the decision boundary. The decision boundaries obtained for apical segments is more reliable than those obtained for mid-cavity and basal slices. This is expected given the fact that the image features within the apical segments are not affected by the papillary muscles.

<sup>4</sup>As suggested by [3], the attachment of the right ventricular wall to the LV is used to identify and separate the septum from the LV anterior and inferior free walls.

<sup>5</sup>Each myocardial segment was marked following a binary score, either normal or abnormal. The ground truth was built by three experienced radiologists, each of whom annotated a different portion of the data set. Among the 928 segments, 579 segments were marked as normal and 349 as abnormal.

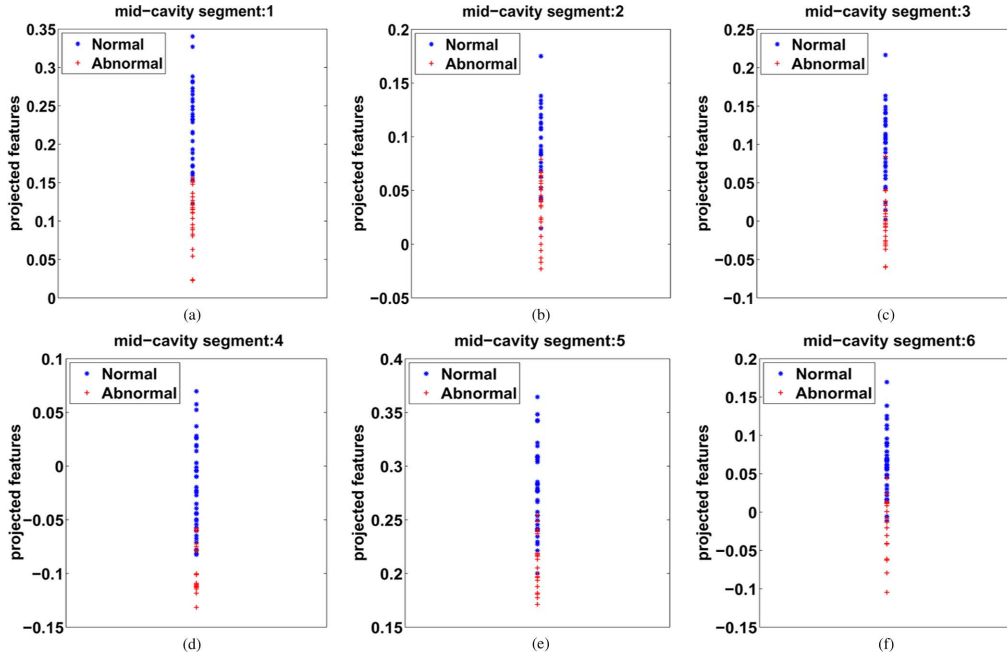


Fig. 14. Projected mid-cavity features ( $\beta_{m,p}^i$ ) obtained following the LDA transformation.

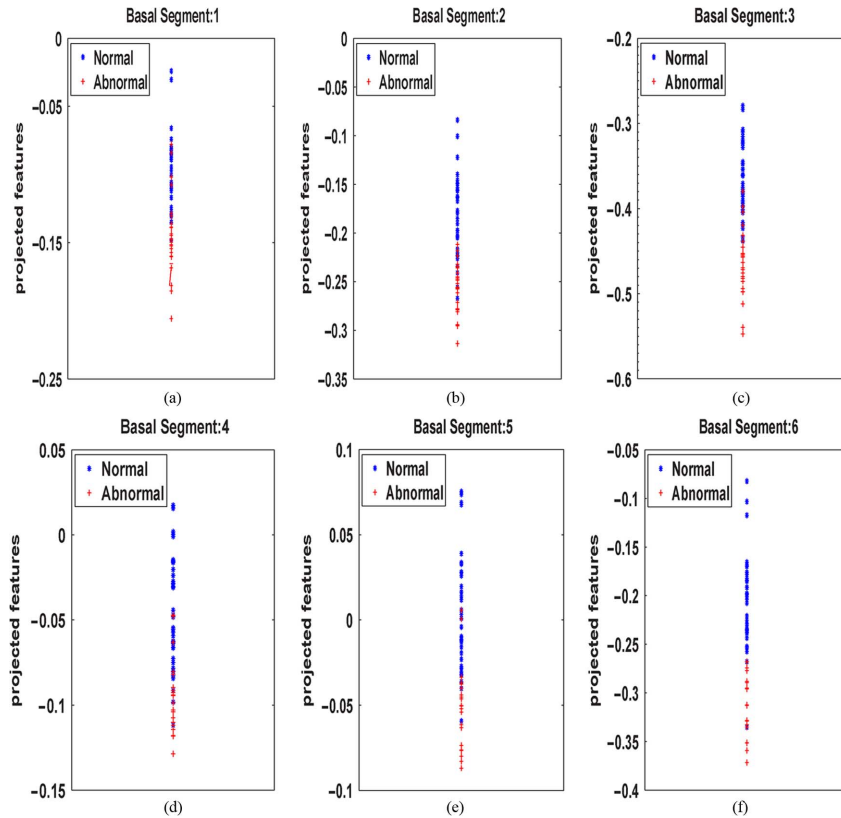


Fig. 15. Projected basal features ( $\beta_{m,p}^i$ ) obtained following the LDA transformation.

#### D. Classification Performance

We used two types of criteria to measure the performance of each classifier: 1) the receiver operating characteristic (ROC) curves with the corresponding area under the curve (AUC) and

2) the Bhattacharyya measure [30] to assess the discriminative power of the features. Furthermore, we assessed the classifier performance with a leave-one-third-of-the-subjects-out approach, i.e., by training our algorithm using 2/3 of the dataset and testing on the remaining data.

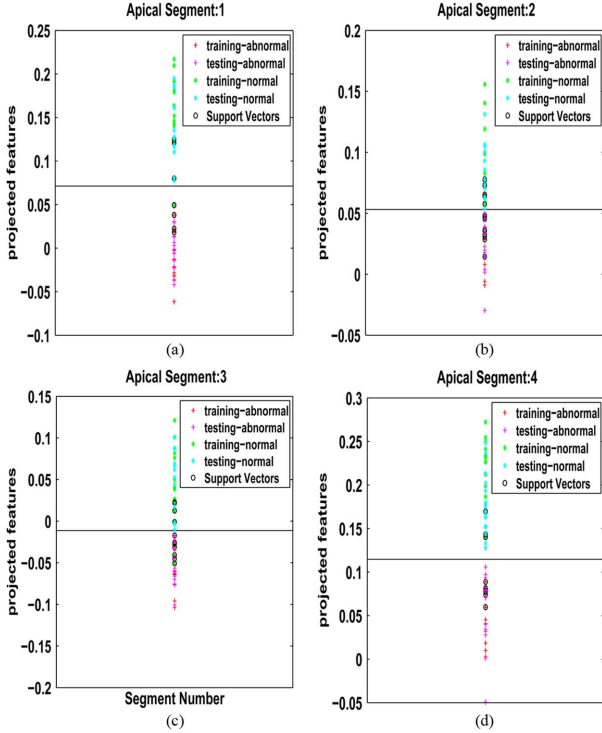


Fig. 16. Decision boundaries and support vectors for the apical segments.

1) *ROC/AUC*: The ROC curves depicted in Figs. 19–21 demonstrate the performances of the proposed method. The best performance is obtained for apical segments. Table II reports the corresponding AUCs.

2) *Bhattacharyya Measure*: We used the Bhattacharyya distance metric to evaluate the overlap between the distributions of features over normal and abnormal classes

$$\mathcal{B} = \sqrt{1 - \sum \sqrt{f_N(y)f_A(y)}} \quad (18)$$

where  $f_N(y)$  and  $f_A(y)$  are the distributions over normal and abnormal hearts, respectively. The higher  $\mathcal{B}$ , the more discriminative the classifier. The Bhattacharyya distances obtained in Table II are consistent with the ROC/AUC evaluations.

3) *Classification Accuracy*: We evaluated the classifier performance by computing the accuracy, specificity, and sensitivity over all the datasets

$$\text{accuracy} = \frac{T_P + T_N}{P + N}, \quad \text{specificity} = \frac{T_N}{N}, \quad \text{sensitivity} = \frac{T_P}{P} \quad (19)$$

where  $T_P$  denote true positives (number of segments correctly classified as “Abnormal”), and  $T_N$  true negatives (number of segments correctly classified as “Normal”). The total number of “Abnormal” and “Normal” segments are  $P$  and  $N$ , respectively.

Table III reports an overall classification accuracy of 86.09%, with a sensitivity of 93.96% and a specificity of 81.82%. The highest performance was achieved for apical slices with 89.75% for accuracy, 94.10% for sensitivity, and 86.29% for specificity.

To show the benefit of combining LDA and SVM in our case, we further evaluated the performance of the algorithm without the dimensionality reduction step, i.e., we applied the SVM

classifier to the full feature set. Table IV reports the obtained performance. The overall classification accuracy decreased to 71.03%, with a sensitivity of 81.56% and a specificity of 61.88%. These results demonstrate that the combination of LDA and SVM yields a significant improvement in accuracy over applying SVM to the initial feature set. Such combination makes sense when the number of samples is not large enough to learn the correlation between the features. Recall that, in our case, each segment has 20 features and 58 samples. As the number of samples is not sufficient to learn the correlation between 20-dimensional features, we proceeded to a dimensionality reduction. Such LDA/SVM combination is also consistent with several prior-art studies in pattern classification. For instance, in [31]–[33], the authors investigated such combination and showed that LDA reflects *global* properties of the class distribution whereas SVM is based on *local* properties of the dataset. As LDA/SVM combination reflects both local and global properties of the features, it is not surprising that it can perform well in our case.

Table V reports comparisons of the obtained results to visual scores by experienced radiologists. We computed the Kappa statistic [34] between the proposed method and radiologists’ findings. The Kappa statistic is given by

$$\kappa = \frac{p(a) - p(e)}{1 - p(e)} \quad (20)$$

where  $p(a)$  is the observed percentage agreement

$$p(a) = \frac{T_P + T_N}{P + N} \quad (21)$$

and  $p(e)$  is the overall probability of random agreement

$$p(e) = \frac{P}{P + N} \frac{T_P + F_N}{P + N} + \frac{N}{P + N} \frac{F_P + T_N}{P + N} \quad (22)$$

$F_P$  denotes false positives (number of segments incorrectly classified as “Abnormal”), and  $F_N$  false negatives (number of segments incorrectly classified as “Normal”). We obtained a kappa statistic of 0.73, a value which indicates a substantial agreement [34] between the proposed method and visual scoring.

#### E. Comparison With Other Methods

Table VI compares the proposed method with several other recent methods with respect to the user-input/segmentation requirements, accuracy, processing time, size of the used data sets, and types of the processed slices. In the second column, the description “manual-first” means that the corresponding method requires a manual segmentation of the first frame, while “manual-all” means that manual segmentations are required for all frames. “Reg” means that the corresponding method requires an inter-frame registration process so as to find the LV boundaries in all the frames of a sequence. In the last column, A, B, and M denote apical, basal, and mid-cavity, respectively. All the methods in Table VI analyze apical, basal and midcavity slices except the method proposed by Lu *et al.* [7] which shows preliminary results for basal slices only.

*User-Inputs/Segmentations*: The proposed method requires manual segmentation of a single frame as user input. On the

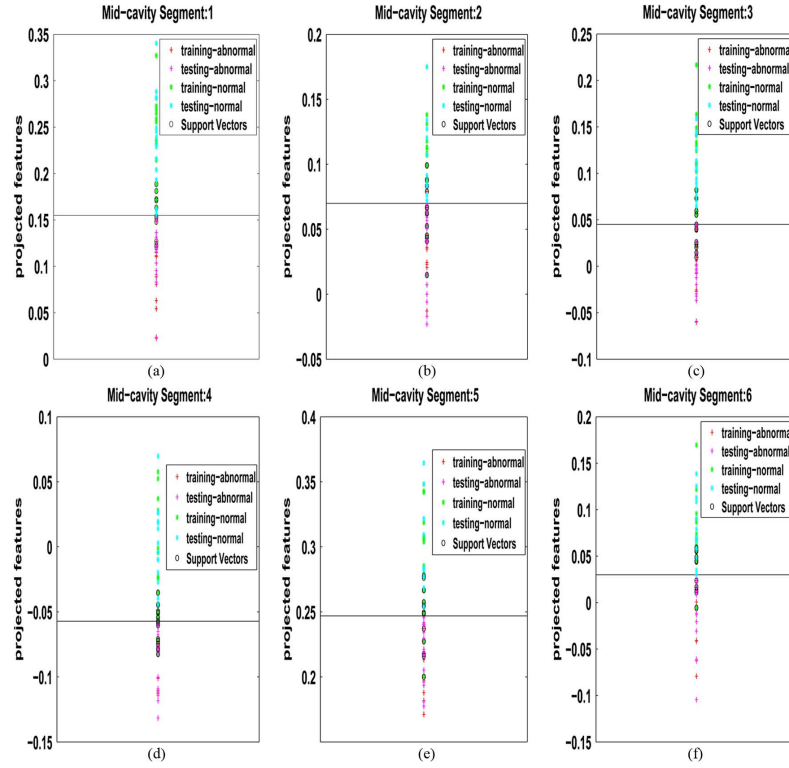


Fig. 17. Decision boundaries and support vectors for the mid-cavity segments.

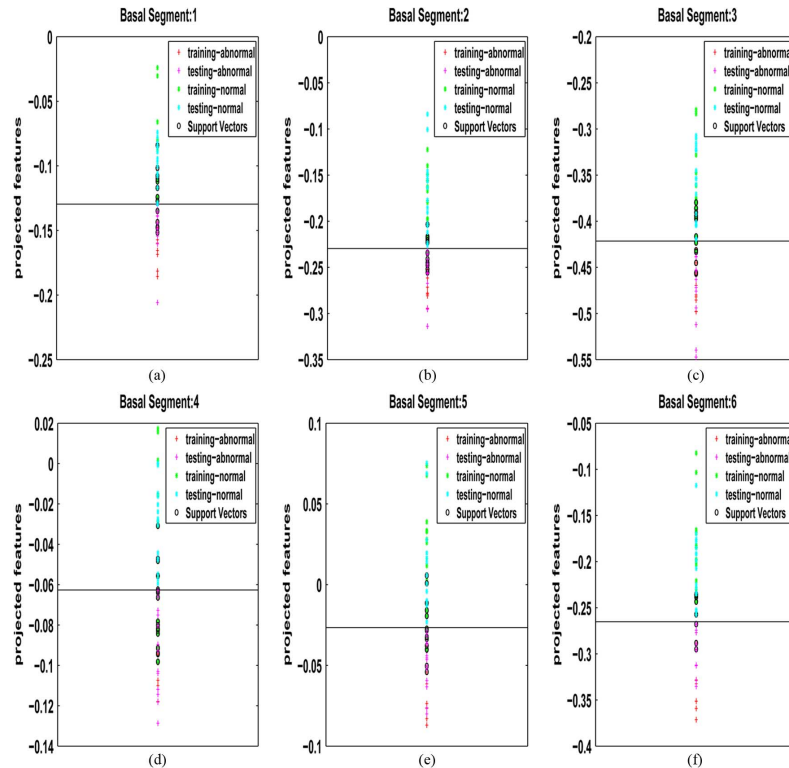


Fig. 18. Decision boundaries and support vectors for the basal segments.

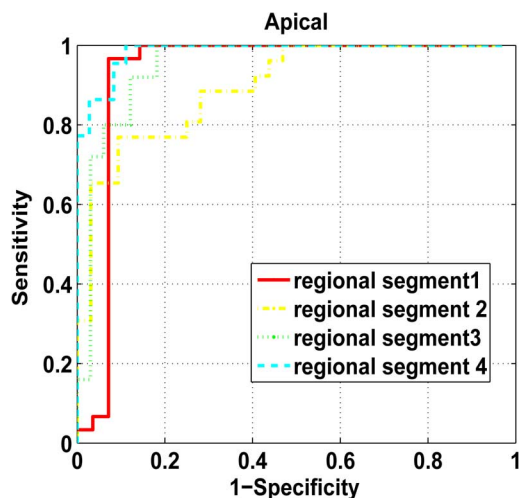


Fig. 19. ROCs for apical segments: the closer the curve to the left-hand top corner, the better the classification performance.

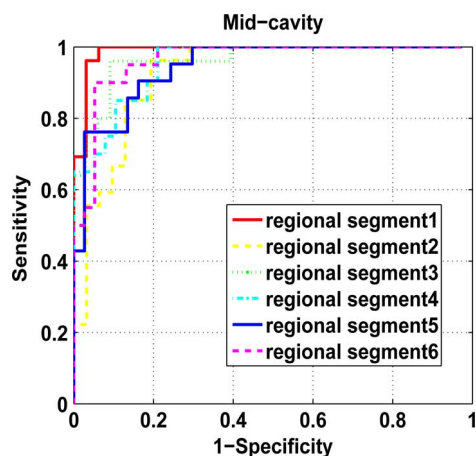


Fig. 20. ROCs for mid-cavity segments: the closer the curve to the left-hand top corner, the better the classification performance.

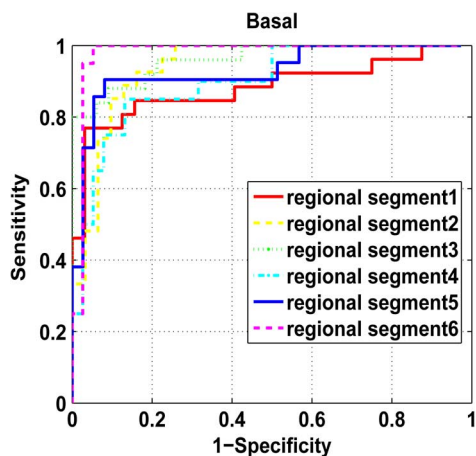


Fig. 21. ROCs for basal segments: the closer the curve to the left-hand top corner, the better the classification performance.

other hand, Punithakumar *et al.* [10], [35] use a manual segmentation of the first frame, and propagate this result via a registration algorithm to obtain the epicardial boundaries in all

TABLE II  
AUCs CORRESPONDING TO FIGS. 19–21 AND THE CORRESPONDING BHATTACHARYYA DISTANCE METRICS ( $\mathcal{B}$ ) OF NORMAL/ABNORMAL DISTRIBUTIONS. THE HIGHER THE VALUES, THE MORE DISCRIMINATIVE THE ABILITY OF THE CLASSIFIER

	AUC	Bhattacharyya distance metric ( $\mathcal{B}$ )
Apical	0.96	0.78
Mid-cavity	0.94	0.69
Basal	0.92	0.63

TABLE III  
CLASSIFICATION ACCURACY USING A LEAVE-ONE-THIRD-OF-THE-SUBJECTS-OUT APPROACH. PROPOSED METHOD ACHIEVED AN OVERALL CLASSIFICATION ACCURACY OF 86.09%

	Sensitivity (%)	Specificity (%)	Accuracy (%)
Apex	94.10	86.29	89.75
Mid-cavity	94.07	80.16	85.72
Base	93.72	78.45	84.02
Overall	93.96	81.82	86.09

TABLE IV  
CLASSIFICATION ACCURACY WITHOUT THE DIMENSIONALITY REDUCTION STEP (i.e., WE APPLIED THE SVM CLASSIFIER TO THE FULL FEATURE SET)

	Sensitivity (%)	Specificity (%)	Accuracy (%)
Apex	82.51	61.75	71.64
Mid-cavity	82.66	57.33	69.51
Base	79.83	66.52	72.16
Overall	81.56	61.88	71.03

TABLE V  
COMPARISONS BETWEEN THE PROPOSED METHOD AND VISUAL ASSESSMENT SCORING BY EXPERIENCED RADIOLOGISTS. PROPOSED METHOD YIELDED A KAPPA MEASURE OF 0.73, A *substantial agreement* WITH RADIOLOGISTS' RESULTS

	Visual assessment by radiologists		
	Abnormal detection	Normal detection	Total
The proposed method			
Abnormal detection	<b>348</b>	89	437
Normal detection	33	<b>458</b>	491
Total	381	547	928

the remaining frames. Similarly, Suinesiaputra *et al.* [15] use manual segmentations in end-diastolic and end-systolic frames followed by a registration algorithm to find the myocardium boundaries in the remaining frames. Garcia-Barnes *et al.* [36] use manual segmentation of the first frame followed by a B-spline registration applied to the myocardium boundaries in all frames. Lu *et al.* [7] show preliminary results for only basal slices; in this method, each of the epicardial boundaries is obtained from manual mouse clicks and spline interpolation. Similarly, the works in [6] and [8] need manual segmentations of all the frames as user inputs.

*Accuracy/Speed:* The meta-analysis of accuracy in Table VI shows that the proposed method can yield a competitive performance while reducing the computational load and user efforts.

TABLE VI

COMPARISONS OF THE PROPOSED METHOD WITH RECENT EXISTING METHODS OF REGIONAL MYOCARDIAL ABNORMALITY DETECTION. ALL THE EXISTING METHODS REQUIRE EITHER MANUAL OR AUTOMATIC (REGISTRATION-BASED) SEGMENTATIONS OF SEVERAL FRAMES IN A CARDIAC SEQUENCE

Method	User-input/Reg	Accuracy	Time	Dataset	slice
Proposed method	mnl-first	0.86	0.15 sec	58 subj cine MRI	A,B,M
Punithakumar <i>et al.</i> [10], [35]	mnl-first + Reg	0.87	62 sec	58 subj cine MRI	A,B,M
Suinesiaputra <i>et al.</i> [15]	mnl-first + Reg	0.78	N/A	53 subj CE MRI	A,B,M
Garcia-Barnes <i>et al.</i> [36]	mnl-first+Reg	0.85	N/A	28 subj Tagged MR	A,B,M
Suinesiaputra <i>et al.</i> [8]	mnl-all	0.77	N/A	89 subj cine MRI	A,B,M
Lu <i>et al.</i> [7]	mnl-all	0.86	N/A	17 subj cine MRI	B
Qian <i>et al.</i> [6]	mnl-all	0.87	N/A	22 subj Tagged MR	A,B,M

## VII. CONCLUSION

We proposed a real-time machine-learning and image-statistic based approach to automating the detection and localization of segmental (regional) myocardial abnormalities in MRI. Unlike the existing techniques, the proposed method did not require delineations of the endo- and/or epi-cardial boundaries in all the frames of a cardiac sequence. Starting from a minimum user input in only one frame in a subject data set, we built a set of statistical MRI features, based on the Bhattacharyya measure of similarity between distributions, for all the regional segments and all subsequent frames. We demonstrated via synthetic and real examples that, over a cardiac cycle, such statistical features are related to the proportion of blood within each segment, and can therefore characterize segmental contraction at a much lower cost in terms of both computation and user effort. We sought the optimal direction along which the proposed image features are most descriptive via an LDA. Then, using these results as inputs to a LSVM classifier, we obtained an abnormality assessment of each of the standard cardiac segments in real-time. We reported a comprehensive experimental evaluation of the proposed algorithm over 928 cardiac segments obtained from 58 subjects. Compared to ground-truth evaluations by experienced radiologists, the proposed algorithm yielded an overall classification accuracy of 86.09% and a kappa measure of 0.73. We further reported meta-analysis comparisons with several recent methods, which showed that the proposed method can yield a competitive performance, while significantly reducing the computational load and user effort.

It is worth noting that the proposed method assumes the global/local motion between two frames is not substantial. Such an assumption may not be valid for abnormal hearts, which undergo twisting motion and/or large shifts in short- or long-axis direction. In such cases, the proposed features may not fully characterize regional motion abnormality. A possible extension would be to investigate the use of motion features.

Another possible extension of the proposed algorithm would be to apply a segmentation algorithm [16] to the first frame so as to fully automate the process.

## REFERENCES

- [1] G. S. Bleumink, A. M. Knetsch, M. C. Sturkenboom, S. M. Straus, A. Hofman, J. W. Deckers, J. C. Witteman, and B. H. Stricker, "Quantifying the heart failure epidemic: Prevalence, incidence rate, lifetime risk and prognosis of heart failure—The Rotterdam study," *Eur. Heart J.*, vol. 25, pp. 1614–1619, 2004.
- [2] G. Buckberg, "Left ventricular form and function: Scientific priorities and strategic planning for development of new views of disease," *Circulation*, vol. 110, pp. e333–e336, 2004.
- [3] M. D. Cerqueira, N. J. Weissman, V. Dilsizian, A. K. Jacobs, S. Kaul, W. K. Laskey, D. J. Pennell, J. A. Rumberger, T. Ryan, and M. Verani, "Standardized myocardial segmentation and nomenclature for tomographic imaging of the heart: A statement for healthcare professionals from the cardiac imaging committee of the council on clinical cardiology of the American Heart Association," *Circulation*, vol. 105, no. 4, pp. 539–542, 2002.
- [4] R. Hoffmann, S. von Bardeleben, J. D. Kasprzak, A. C. Borges, F. ten Cate, C. Firsckhe, S. Lafitte, N. Al-Saadi, S. Kuntz-Hehner, G. Horstick, C. Greis, M. Engelhardt, J. L. Vanoverschelde, and H. Becher, "Analysis of regional left ventricular function by cineventriculography, cardiac magnetic resonance imaging, and unenhanced and contrast-enhanced echocardiography: A multicenter comparison of methods," *J. Am. Coll. Cardiol.*, vol. 47, no. 1, pp. 121–128, 2006.
- [5] A. B. Redheuil, N. Kachenoura, R. Laporte, A. Azarine, X. Lyon, O. Jolivet, F. Frouin, and E. Mousseaux, "Interobserver variability in assessing segmental function can be reduced by combining visual analysis of CMR cine sequences with corresponding parametric images of myocardial contraction," *J. Cardiovas. Magn. Reson.*, vol. 9, no. 6, pp. 863–872, 2007.
- [6] Z. Qian, Q. Liu, D. N. Metaxas, and L. Axel, "Identifying regional cardiac abnormalities from myocardial strain using spatio-temporal tensor analysis," in *Proc. MICCAI 2008*, 2008, vol. 5241, pp. 789–797.
- [7] Y. Lu, P. Radau, K. Connelly, A. Dick, and G. Wright, "Pattern recognition of abnormal left ventricle wall motion in cardiac MR," in *Proc. MICCAI 2009*, 2009, vol. 5762, pp. 750–758.
- [8] A. Suinesiaputra, A. Frangi, T. Kaandorp, H. Lamb, J. Bax, J. Reiber, and B. Lelieveldt, "Automated detection of regional wall motion abnormalities based on a statistical model applied to multislice short-axis cardiac MR images," *IEEE Trans. Med. Imag.*, vol. 28, no. 4, pp. 595–607, Apr. 2009.
- [9] J. Garcia-Barnes, D. Gil, L. Badiella, A. Hernandez-Sabate, F. Carreras, S. Pujades, and E. Marti, "A normalized framework for the design of feature spaces assessing the left ventricular function," *IEEE Trans. Med. Imag.*, vol. 29, no. 3, pp. 733–745, Mar. 2010.
- [10] K. Punithakumar, I. B. Ayed, A. Islam, I. G. Ross, and S. Li, "Regional heart motion abnormality detection via information measures and unscented Kalman filtering," in *Proc. MICCAI 2010*, 2010, vol. 6361, pp. 409–417.
- [11] K. Lekadir, N. Keenan, D. Pennell, and G. Yang, "An inter-landmark approach to 4-d shape extraction and interpretation: Application to myocardial motion assessment in MRI," *IEEE Trans. Med. Imag.*, vol. 30, no. 1, pp. 52–68, Jan. 2011.
- [12] J. G. Bosch, F. Nijland, S. C. Mitchell, B. P. Lelieveldt, O. Kamp, J. H. Reiber, and M. Sonka, "Computer-aided diagnosis via model-based shape analysis: Automated classification of wall motion abnormalities in echocardiograms," *Acad. Radiol.*, vol. 12, no. 3, pp. 358–367, 2005.
- [13] K. Y. Leung and J. G. Bosch, "Localized shape variations for classifying wall motion in echocardiograms," in *Proc. MICCAI 2007*, 2007, vol. 4791, pp. 52–59.
- [14] S. Mansor and J. Noble, "Local wall motion classification of stress echocardiography using a hidden Markov model approach," in *Proc. IEEE Int. Symp. Biomed. Imag.: From Nano to Macro*, 2008, pp. 1295–1298.
- [15] A. Suinesiaputra, A. F. Frangi, T. A. Kaandorp, H. J. Lamb, J. J. Bax, J. H. Reiber, and B. P. Lelieveldt, "Automated regional wall motion abnormality detection by combining rest and stress cardiac MRI: Correlation with contrast-enhanced MRI," *J. Magn. Reson. Imag.*, vol. 34, no. 2, pp. 270–278, 2011.

- [16] C. Petitjean and J.-N. Dacher, "A review of segmentation methods in short axis cardiac MR images," *Med. Image Anal.*, vol. 15, no. 2, pp. 169–184, 2011.
- [17] M. Afshin, I. Ben Ayed, K. Punithakumar, M. W. K. Law, A. Islam, A. Goela, I. G. Ross, T. M. Peters, and S. Li, "Assessment of regional myocardial function via statistical features in MR images," in *Proc. MICCAI 2011*, 2011, vol. 6893, pp. 107–114.
- [18] O. Michailovich, R. Yogesh, and A. Tannenbaum, "Image segmentation using active contours driven by the Bhattacharyya gradient flow," *IEEE Trans. Image Process.*, vol. 16, no. 11, pp. 2787–2801, Nov. 2007.
- [19] I. Ben Ayed, S. Li, and I. Ross, "A statistical overlap prior for variational image segmentation," *Int. J. Comput. Vis.*, vol. 85, no. 1, pp. 115–132, 2009.
- [20] J. Ye, R. Janardan, Q. Li, and H. Park, "Feature reduction via generalized uncorrelated linear discriminant analysis," *IEEE Trans. Knowl. Data Eng.*, vol. 18, no. 10, pp. 1312–1322, Oct. 2006.
- [21] G. C. Lin, W. J. Wang, C. M. Wang, and S. Y. Sun, "Automated classification of multi-spectral MR images using linear discriminant analysis," *Comput. Med. Imag. Graph.*, vol. 34, pp. 251–268, 2010.
- [22] P. Xu, G. N. Brock, and R. S. Parrish, "Modified linear discriminant analysis approaches for classification of high-dimensional microarray data," *Computat. Stat. Data Anal.*, vol. 53, pp. 1674–1687, 2009.
- [23] Y.-C. Yeh, W.-J. Wang, and C. W. Chiou, "Cardiac arrhythmia diagnosis method using linear discriminant analysis on ecg signals," *Measurement*, vol. 42, pp. 778–789, 2009.
- [24] H.-C. Kim, D. Kim, and S. Y. Bang, "Face recognition using LDA mixture model," *Pattern Recognit. Lett.*, vol. 24, pp. 2815–2821, 2003.
- [25] G. Mercier and M. Lennon, "Support vector machines for hyperspectral image classification with spectral-based kernels methods," in *Proc. IEEE Int. Geosci. Remote Sens. Symp.*, 2003, pp. 288–290.
- [26] Y. H. Liu, H. P. Huang, and C. H. Weng, "Recognition of electromyographic signals using cascaded kernel learning machine," *IEEE-ASME Trans. Mechatron.*, vol. 12, pp. 253–264, 2007.
- [27] K. Polat, S. Güneş, and A. Arslan, "A cascade learning system for classification of diabetes disease: Generalized discriminant analysis and least square support vector machine," *Expert Syst. Appl.*, vol. 34, pp. 482–487, 2008.
- [28] K. Polat and S. Güneş, "A novel approach to estimation of e. coli promoter gene sequences: Combining feature selection and least square support vector machine," *Appl. Math. Computat.*, vol. 190, no. 2, pp. 1574–1582, 2007.
- [29] C. M. Bishop, *Pattern Recognition and Machine Learning*, 1st ed. New York: Springer-Verlag, 2006.
- [30] D. Comaniciu, V. Ramesh, and P. Meer, "Kernel-based object tracking," *IEEE Trans. Pattern Anal. Mach. Intell.*, vol. 25, no. 5, pp. 564–577, May 2003.
- [31] T. Xiong and V. Cherkassky, "A combined SVM and LDA approach for classification," in *Proc. IEEE Int. Joint Conf. Neural Netw.*, 2005, vol. 3, pp. 1455–1459.
- [32] J. Peng, D. Heisterkamp, and H. K. Dai, "LDA/SVM driven nearest neighbor classification," *IEEE Trans. Neural Netw.*, vol. 14, no. 4, pp. 940–942, Jul. 2003.
- [33] Z. Wang and X. Qian, "Text categorization based on LDA and SVM," in *Proc. Int. Conf. Comput. Sci. Software Eng.*, 2008, vol. 1, pp. 674–677.
- [34] A. J. Viera and J. M. Garret, "Understanding interobserver agreement: The kappa statistic," *Family Med.*, vol. 37, no. 5, pp. 360–363, 2005.
- [35] K. Punithakumar, I. B. Ayed, A. Islam, A. Goela, I. G. Ross, J. Chong, and S. Li, "Regional heart motion abnormality detection: An information theoretic approach," *Med. Image Anal.*, vol. 17, no. 3, pp. 311–324, 2013.
- [36] J. Garcia-Barnes, D. Gil, L. Badiella, A. Hernández-Sabaté, F. Carreras, S. Pujadas, and E. Martí, "A normalized framework for the design of feature spaces assessing the left ventricular function," *IEEE Trans. Med. Imag.*, vol. 29, no. 3, pp. 733–745, Mar. 2010.